Magnetic Resonance in Medicine 54:850–859 (2005)

Ex Vivo 3D Diffusion Tensor Imaging and Quantification of Cardiac Laminar Structure

Patrick A. Helm,[1*] Hsiang-Jer Tseng,[1] Laurent Younes,[2] Elliot R. McVeigh,[3] and Raimond L. Winslow[1]

A three-dimensional (3D) diffusion-weighted imaging (DWI) method for measuring cardiac fiber structure at high spatial resolution is presented. The method was applied to the ex vivo reconstruction of the fiber architecture of seven canine hearts. A novel hypothesis-testing method was developed and used to show that distinct populations of secondary and tertiary eigenvalues may be distinguished at reasonable confidence levels ($P \leq 0.01$) within the canine ventricle. Fiber inclination and sheet angles are reported as a function of transmural depth through the anterior, lateral, and posterior left ventricle (LV) free wall. Within anisotropic regions, two consistent and dominant orientations were identified, supporting published results from histological studies and providing strong evidence that the tertiary eigenvector of the diffusion tensor (DT) defines the sheet normal. Magn Reson Med 54:850–859, 2005. Published 2005 Wiley-Liss, Inc.†

Key words: diffusion tensor MRI; myocardial microstructure; anisotropic diffusion; myofiber laminar sheets; cardiac

The myocardial microstructure has been demonstrated to play an important role in both mechanical and electrical function of the ventricles. The microstructure influences transmural stress during mechanical contraction (1). Studies of cardiac mechanics have indicated that during the cardiac cycle there is substantial reorientation of the laminar architecture, and that this reorientation is both local and load dependent (2). Studies of electrical activation patterns have shown that current propagates most rapidly in the direction of the longitudinal fiber axis, and that spatial change of fiber orientation influences conduction properties (3–5). Remodeling of both ventricular geometry and fiber organization is a prominent feature of cardiac pathologies (6). A detailed knowledge of ventricular fiber structure, including how it may be remodeled in cardiac pathology and the effects of this remodeling on ventricular conduction and mechanical function, is therefore fundamentally important for understanding the nature of cardiac electromechanics in healthy and diseased hearts.

Over the last decade, developments in diffusion tensor MRI (DTI) have permitted the noninvasive measurement of the self diffusion of water through tissue. The diffusion of water molecules driven by their thermal energy is restricted by the tissue microstructure. In fibrous tissue, water diffuses preferentially in the fiber direction. Basser et al. (7) showed that a symmetric tensor representing the mean path of water diffusion may be computed from multiple images obtained with different gradient weightings. By comparing the principle eigenvector of the DT at each image voxel with the fiber orientation measured histologically, one can see that the principle direction of water diffusion in cardiac tissue is parallel to the fiber long axis (8–10). More recently, it was also suggested that the secondary and tertiary eigenvectors of the DT correlate with the laminar structure of the ventricles (11,12), with the tertiary eigenvector defining the surface normal to the laminar sheets. However, evidence suggests that in the myocardium, the secondary and tertiary eigenvalues are similar in magnitude. Pierpaoli et al. (13) showed that under those conditions and in the presence of noise, the rotationally invariant diffusion indices that describe anisotropic diffusion and require sorting of eigenvalues based on their magnitude are statistically biased. For example, the ratio between the largest and smallest eigenvalues ($\lambda 1/\lambda 3$) is particularly susceptible to sorting error. Furthermore, once the eigenvalues are sorted, the assumptions of random sampling are violated and therefore standard statistical tests are no longer valid (13). This "sorting bias" (i.e., incorrect classification of secondary vs. tertiary eigenvalues) also introduces a bias in the mean and variance of the sample eigenvectors (principle directions), and degrades the characterization of tissue anisotropy (14,15). The complexity of the cardiac architecture combined with errors in classifying the secondary and tertiary eigenvalues and eigenvectors presents a significant challenge to investigators who seek to measure laminar structure using DTI.

The purpose of this work was to extend the two-dimensional (2D) fast spin echo (FSE) and 2D multislice SE (2D MSE) DTI methods used in previous studies to a three-dimensional (3D) FSE DTI method for high-spatial-resolution imaging of cardiac microstructure. We use a statistical approach to identify secondary vs. tertiary eigenvalues, and show that three distinct populations of eigenvalues exist in various anatomical regions of the canine ventricles. Within these regions eigenvectors may be classified according to the eigenvalue magnitude with minimal error. We use a finite element (FE) representation of the geometry constructed from the MR data to study fiber inclination angles in various regions of the heart. Finally, we provide evidence supporting the hypothesis that the tertiary eigenvector correlates with the sheet normal.

[1]Center for Cardiovascular Bioinformatics and Modeling, Johns Hopkins University, Baltimore, Maryland, USA.

[2]Center for Imaging Science, Johns Hopkins University, Baltimore, Maryland, USA.

[3]Laboratory of Cardiac Energetics, National Heart, Lung, and Blood Institute, National Institutes of Health, Bethesda, Maryland, USA.

Grant sponsor: NIH; Grant numbers: HL70894; HL52307; Grant sponsors: Falk Medical Trust; IBM Corporation.

*Correspondence to: Patrick A. Helm, Department of Biomedical Engineering, Johns Hopkins University School of Medicine, 202 Clark Hall, 3400 North Charles Street, Baltimore, MD 21218. E-mail: phelm@bme.jhu.edu

Received 28 July 2004; revised 25 April 2005; accepted 5 May 2005.

DOI 10.1002/mrm.20622

Published online 7 September 2005 in Wiley InterScience (www.interscience.wiley.com).

MATERIALS AND METHODS

Isolation and Fixation of Hearts

The seven adult male beagle dogs used in this study were also used in previous mechanical mapping studies (16). All aspects of these studies were conducted in accordance with the guidelines of the Animal Care and Use Committee of the National Heart, Lung, and Blood Institute. Anesthesia was induced with sodium thiopental and maintained after intubation with isoflurane. A midline thoracotomy was performed. The animals were heparinized, and cardiac arrest was induced with a bolus of potassium chloride. Following explantation, a Langendorff preparation was used to perfuse the hearts with saline solution until the coronary vessels were clear. To maintain diastolic conformation during imaging, vinyl polysiloxane (3M Corp., St. Paul, MN, USA) was injected into each of the four chambers via the tricuspid and mitral valves. The hearts were then perfused with and stored in a 7% by volume isotonic solution of formaldehyde. The hearts were fixed in the same cardiac phase so that the fiber orientations would be similar. Small variations in cardiac phase during fixation are not problematic because fiber angles do not change significantly between diastole and systole (17).

MR Preparation for Whole-Heart Imaging

Each heart was placed in an acrylic container filled with Fomblin, a perfluoropolyether (Ausimon, Thorofare, NJ). The low dielectric effect and minimal MR signal of Fomblin increases contrast and eliminates unwanted susceptibility artifacts near the boundaries of the heart. The long axis of each heart was aligned with the *z*-axis of the scanner. Images were acquired with a four-element phased array coil on a 1.5 T GE CV/I MRI scanner (GE, Medical System, Wausheka, WI, USA) with an enhanced gradient system. The system had a 40 mT/m maximum gradient amplitude and a 150 T/m/s slew rate. The hearts were placed in the center of the coil, and a 3D-FSE sequence was used to acquire diffusion images.

DTI

Basser et al. (7) developed a DTI method to quantify diffusion in an anisotropic environment (7). The tensor defines the extent of water diffusion along any desired direction at each voxel in the image. The DT **D** is related to the MR signal by the following equation:

$$\ln\left(\frac{S(b)}{S(0)}\right) = \sum_{i=1}^{3}\sum_{j=1}^{3} - b_{ij}D_{ij} \qquad [1]$$

where $S(0)$ is the MR signal intensity with no diffusion gradients, and $S(b)$ is the signal with the application of the diffusion weight b. The diffusion-weighting factor b is a matrix that is computed analytically for a given sequence of field gradient pulses (8). The DT is symmetric and thus a minimum of six experiments with independent diffusion weightings plus one reference image with zero diffusion weighting $S(0)$ are necessary to estimate the tensor (7). The eigenvalues and eigenvectors of this tensor were identified and used to predict structural properties of the tissue. (All of the DTI data sets employed in this study are available at www.ccbm.jhu.edu.)

Measurements of fixed myocardium T_1 and T_2 relaxation parameters were conducted to aid in the selection of the diffusion imaging parameters. T_1 measurements were conducted with an inversion recovery spin-echo (SE) sequence, while T_2 parameters were estimated using a SE sequence with varying TE.

We developed a 3D FSE DTI pulse sequence by modifying a 3D FSE sequence (18,19). The diffusion encoding was produced using a pair of gradient pulses placed symmetrically around the first 180° RF pulse. Gradient pulses were 20 ms in duration, with a trapezoidal shape. Phase encoding was applied in both the *y* and *z* directions to generate 3D image data. Because of the long duration of the diffusion gradients and the short T_2 of fixed myocardium ($T_2 \sim 65$ ms; see Results), only two echoes were used. MR parameters varied slightly depending on heart size. The FOV was ~8 cm with an image size of 192 × 192 zero-padded to 256 × 256. The volume was imaged with 110–120 slices at ~800 μm thickness. The diffusion gradients were applied in a minimum of 16 noncollinear directions with a maximum *b*-value of 1500 s/mm^2. Two null weighted images were also obtained, yielding a minimum of 18 volume acquisitions. Since only two echoes were used, the *b*-value correction for the echo train was minimal and thus was not taken into account (20). The total scan time was approximately 40 hrs with a TR of 700 ms.

After MRI was performed, the six components of the DT were estimated in each voxel by solving the least-squares problem defined in Eq. [1]. The tensors' eigenvalues and eigenvectors were then computed using a singular value decomposition (SVD) algorithm (MATLAB, MathWorks, Natick, MA, USA).

Classification of Eigenvectors

It has been suggested that the tertiary eigenvector of diffusion is a surface normal to the ventricular laminar sheet (11). Identification of the tertiary eigenvector of the DT at each imaging voxel requires that diffusivity be estimated in the plane orthogonal to the primary eigenvector of the DT. Two cases must be considered: 1) equal diffusivities in the orthogonal directions of this plane (transverse isotropic diffusion), and 2) unequal diffusivities in the orthogonal directions (transverse anisotropic diffusion). In the former case, the secondary and tertiary eigenvalues are indistinguishable and their corresponding eigenvectors are uniformly distributed about the unit disc normal to the principle axis. The DT cannot be used to infer properties of laminar sheet structure in regions where diffusion is transversely isotropic. It may be possible to infer such properties in the latter case, in which diffusion is transversely anisotropic. Studies have demonstrated an underlying transverse anisotropic structure of cardiac tissue (17,21); however, it is unclear whether anisotropic structure may be inferred reliably from DTI data. In the following sections we describe two hypothesis-testing procedures for identifying regions of myocardium that exhibit anisotropic diffusion under the assumption that myocardium has a locally homogenous microstructure.

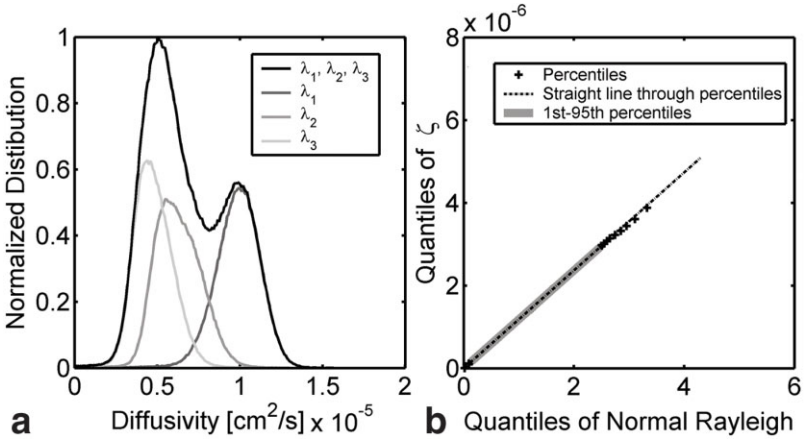

FIG. 1. **a:** Histogram of eigenvalues from a single heart. The solid black line represents a histogram of the unsorted eigenvalues. The grayscale lines represent histograms of the sorted primary, secondary, and tertiary eigenvalues. **b:** qq plot of a normal Raleigh distribution vs. $\zeta = \lambda_2 - \lambda_3$.

Figure 1a shows a histogram of eigenvalues measured using DTI at each myocardial imaging voxel in a canine ventricle (black line). Two peaks are evident. The histogram peak at an approximate diffusivity of 1.0×10^{-5} cm^2/s is associated with the primary eigenvectors of the DTs. The histogram peak at $\sim 0.5 \times 10^{-5}$ cm^2/s represents the diffusivities associated with the secondary and tertiary eigenvectors. Inspection of Fig. 1a shows the secondary and tertiary eigenvalues are similar. As a result, classification of their corresponding eigenvectors based on eigenvalue magnitude may be prone to significant error. Distributions of the primary, secondary and tertiary eigenvalues (grayscales) estimated on the basis of relative magnitude are also shown in Fig. 1a. There is significant overlap between the secondary and tertiary eigenvalue distributions. This overlap will necessarily lead to a significant error rate when eigenvectors are identified based only on the magnitude of their corresponding eigenvalues. Therefore, we developed a statistical method to test the null hypothesis that the secondary and tertiary eigenvalues are equal within a local region of the myocardium (i.e., transverse isotropy). Rejection of the null hypothesis provides confidence in sorting the eigenvalues based on magnitude.

Knowledge of the distribution of eigenvalues is necessary to define the appropriate statistical test for determining whether distinct populations of secondary and tertiary eigenvalues exist. Define Δ as the true difference between the secondary and tertiary eigenvalues (λ_2, λ_3), and ζ as the experimentally measured difference. By definition $\lambda_2 > \lambda_3$, and therefore ζ is strictly positive. Under the assumptions that 1) variation of the first eigenvalue and eigenvector is negligible, 2) the last two eigenvalues are equal, and 3) elements of the DT may be represented as a constant plus an additive Gaussian random variable, it can be shown that ζ has a Rayleigh distribution (22). Quantile-quantile (qq)-plots may be used to test the hypothesis that experimentally observed data are well described using a given distribution. The data are divided into quantiles, where the n^{th} quantile is defined as a value for which at least n percent of the data is less. Figure 1b shows such a plot in which values of a normal Raleigh distribution (abscissa) are plotted vs. values of the experimentally measured data ζ (ordinate; normalized by the variance). The quantiles of these distributions are indicated by crosses. If ζ has a Raleigh distribution, then the data points will lie on a straight line of slope 1. The solid bar represents the 1st–95th quantiles of the samples. Within this region, ζ closely resembles a Raleigh distribution. At higher quantiles the data depart above the line. This characteristic departure is typical of data of distributions with long tails, and indicate that ζ is only approximately Raleigh distributed. Since ζ contains some outliers, we define the measure of deviation as:

$$T = \frac{Mdn(\zeta)}{Mdn(|\zeta - Mdn(\zeta)|)} \quad [2]$$

This measure differs from the standard *t*-test in that the median (Mdn) is used instead of the mean. The mean is useful in constructing this test statistic in cases in which there are few outlying data points. It is more effective to use the median for this statistic in cases in which there are outliers in the data, since the median is less susceptible to them. Monte Carlo simulations were used to define the critical value for rejection of the null hypothesis ($\Delta = 0$, i.e., $\lambda_2 = \lambda_3$). These simulation methods are similar to those used by others (13). Specifically, an ideal tensor with $\Delta = 0$ was defined, and, using Eq. [1], ideal imaging data S were computed from the ideal tensor. Gaussian noise with variance similar to the experimental data was then added to the real and imaginary components of the imaging data. Using Eq. [1], a new tensor was computed from the "noisy" images. This process was repeated multiple times to create a distribution of eigenvalues from which the critical value of the statistical test was determined. We also used these simulations to explore the power of the *t*-test as a function of Δ.

We took the analysis further and defined another test based on the distribution of eigenvectors in a local region. In the case of transverse isotropy, the secondary and tertiary eigenvectors are uniformly distributed about the unit disc normal to the primary eigenvector. Defining α as the angle between some reference vector, V_n, and the secondary eigenvector, V_2,

$$\alpha = \cos^{-1}(|V_2 \cdot V_n|) \quad [3]$$

we defined the measure of uniformity as

$$R = \max_{\theta\varepsilon[0,\pi]}\left(\left|\frac{\theta}{\pi} - F_{\alpha}(\theta)\right|\right) \quad [4]$$

where $F_{\alpha}(\theta)$ is the empirical cumulative distribution function of the angles, α. This measure is similar to the Kolmogorov-Smirnov test (23). In this case, a known data set with uniform distribution is compared with the distribution of α. The reference vector V_n is chosen as a vector that is most orthogonal (V_n is the vector for which the sum of projections onto the set of primary eigenvectors is minimal) to the distribution of primary eigenvectors within the ROI. Eigenvectors that are uniformly distributed about the principle direction (transverse isotropy) will have an R-value close to zero, whereas eigenvectors that are not uniformly distributed (anisotropy) will have a large R-value. As with the t-test, we used Monte Carlo simulations to characterize the critical values and the power of the R-test as a function of Δ. A weakness of the R-test is that V_n is sensitive to noise and natural variation in the distribution of primary eigenvectors within the ROI. Therefore, during the Monte Carlo simulations of this test, it was necessary to include a small variation in the primary eigenvector of the ideal tensor before noise was added.

Finally, estimations of tissue structure by DTI depend on the accuracy and precision of the eigenvectors. Any uncertainty in eigenvector direction weakens our confidence in the measurement of the tissue axes. In our simulations, we define uncertainty of the eigenvectors as the angle between the secondary eigenvector of the ideal tensor (noise free) and the mean vector of simulated secondary eigenvectors. The mean vector is computed using a dyadic formalism to resolve the problem of antipodal symmetry of eigenvectors (14). Therefore, a small angle of uncertainty would indicate that the majority of secondary eigenvectors within an ROI are aligned with the secondary eigenvector of the ideal tensor.

We summarize the methods used to investigate the higher-order components of diffusion in the work flow diagram shown in Fig. 2. As depicted in the figure, parameters from the experimental DT images (specifically the image noise, ROI sample size, and mean diffusivities) were used as inputs to the Monte Carlo simulations. These simulations defined the critical value for rejection of the null hypothesis within the ROI. Eigenvectors in regions where anisotropic diffusion was identified (i.e., the null hypothesis was rejected) were used to study tissue architecture.

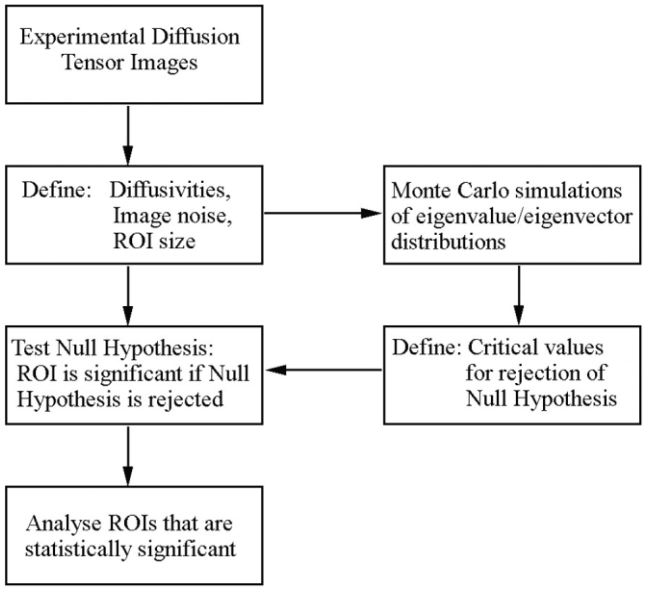

FIG. 2. A work flow diagram of the method used to investigate the higher-order components of diffusion. Experimental DT images define the parameters that are used as inputs to the Monte Carlo simulations. These simulations define the critical value of the t-test for which the null hypothesis may be rejected in a given ROI. Eigenvectors originating from ROIs in which the null hypothesis is rejected are used to infer sheet structure.

Fiber and Geometric Modeling

Since the fiber orientation of the heart is commonly defined with respect to its geometry, the structure of the cardiac ventricles was modeled using 3D FEs defined in a prolate spheroidal coordinate system, as described by Nielsen et al. (24). Initially, the geometry of the heart was modeled using a predefined mesh with eight circumferential elements and four axial elements. These elements used a cubic Hermite interpolation in the transmural direction (φ) and a bilinear interpolation in both the longitudinal (μ) and circumferential (ν) directions. Voxels in the 3D DTI images identified as being on the epicardial and endocardial surfaces by a previously described (11) semiautomated contouring process were used to refine the initial mesh. The Cartesian coordinates of these voxels were first rigidly rotated so that the long axis of the left ventricle (LV) was roughly aligned with the Cartesian z-axis. They were then transformed into prolate spherical coordinates with μ and ν components used to project each data point onto an initial mesh. A linear least-squares algorithm was used to minimize the objective function:

$$\text{Fit error} = \sum_{k=1}^{C} \|\varphi(\mu_k,\nu_k) - \varphi_k\|^2 + \int_{\Omega} g(\varphi(\mu,\nu))\partial\mu\partial\nu \quad [5]$$

$$g(\varphi(\mu,\nu)) = \beta\left(\left\|\frac{\partial\varphi}{\partial\mu}\right\|^2 + \left\|\frac{\partial\varphi}{\partial\nu}\right\|^2\right) + \gamma\left(\left\|\frac{\partial^2\varphi}{\partial\mu^2}\right\|^2 + \left\|\frac{\partial^2\varphi}{\partial\mu\partial\varphi}\right\|^2 + \left\|\frac{\partial^2\varphi}{\partial\nu^2}\right\|^2\right) \quad [6]$$

where C is the number of contour points, φ_k is the φ component of each data point, and $\varphi(\mu_k, \nu_k)$ is the interpolated value of the corresponding data point projected to prolate coordinates (μ_k, ν_k). The second term of the objective function, known as the weighted Sobelov norm, limits the stretching (first derivative terms) and bending (second derivative terms) of the surface (25). The parameters β and γ control the degree of deformation of each element. The weighted Sobelov norm was particularly useful for controlling element deformation in cases in which the contour data were sparse or from highly trabeculated regions. In

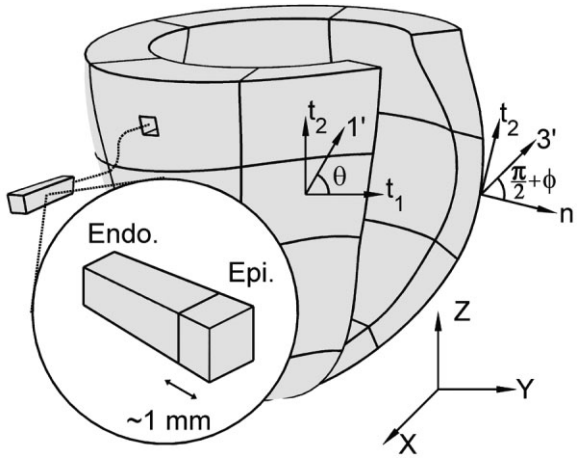

FIG. 3. The coordinate system used to define the inclination angle θ and the intersection angle ϕ. The inclination angle is the angle formed by the circumferential tangent vector $\boldsymbol{T_1}$ and the projection of the primary eigenvector **1′** into the tangent plane defined by vectors $\boldsymbol{T_1}$ and $\boldsymbol{T_2}$. The intersection angle is defined relative to the tertiary eigenvector where $\pi/2 + \phi$ is the angle formed by the surface normal **n** and the projection of the tertiary eigenvector **3′** into the plane defined by vectors $\boldsymbol{T_2}$ and **n**. Transmural regions were isolated as depicted and described in Materials and Methods.

particular, we found it useful for modeling the RV endocardial surfaces. The algorithms for both the geometric fitting and visualization were written in MATLAB 6.1 (MathWorks).

Inferring Structure From the Eigenvectors

The eigenvectors that originated from voxels within the FE boundaries were used to study the fiber structure of the ventricles. These eigenvectors were transformed into local material coordinates of the model as described by LeGrice et al. (21). The inclination angle θ, the angle formed by the circumferential tangent vector $\boldsymbol{T_1}$ and the projection of the primary eigenvectors onto the surface tangent plane defined by vectors $\boldsymbol{T_1}$ and $\boldsymbol{T_2}$, was computed as shown in Fig. 3. The circumferential tangent vector $\boldsymbol{T_1}$ was constrained to the *xy* plane. The eigenvectors were visualized as vectors projected onto the geometric surface. In regions where anisotropic diffusion was identified (i.e., the null hypothesis was rejected), the intersection angle, $\phi \leq \phi \leq \pi$ was defined relative to the tertiary eigenvector of diffusion, where $\pi/2 + \phi$ was the angle formed by the surface normal, **n**, and the projection of the tertiary eigenvector **3′** into the plane defined by the surface normal **n** and axial tangent vector $\boldsymbol{T_2}$ as shown in Fig. 3.

Statistical Analysis of Angles

Circular statistics were used to report all angles. If two dominant populations of angles existed, their means were determined by fitting the bimodal distribution with two wrapped normal distributions (26). The error function for the fit was defined by

$$\text{Fit error} = \int_0^{\pi/2} (P(\phi) - (f_1(\phi) + f_2(\phi)))^2 d\phi \qquad [7]$$

$$f_i(\phi) = \frac{1}{2\pi}\left(1 + 2\sum_{k=1}^{\infty} \rho_i^{k^2} \cos\left(2k(\phi - \hat{\phi}_i)\right)\right) \qquad [8]$$

where $P(\phi)$ represents the distribution of the experimental data, and $f_i(\phi)$ represents a wrapped normal distribution with mean $\hat{\phi}_i$ and variance ρ_i. The error function was minimized using an unconstrained nonlinear minimization algorithm to determine the means of the two populations, $\hat{\phi}_1$ and $\hat{\phi}_2$. Each bimodal distribution was fit multiple times with a different percentage of noise added to the estimated means ϕ_i and variances ρ_i. Local minima were avoided if the solutions converged to the same value, which occurred in most cases.

RESULTS

The T_2 and T_1 relaxation constants for fixed myocardium were estimated at ~65.1 ± 14.2 ms and 410.1 ± 116.9 ms, respectively. Seven normal canine hearts were imaged with a 3D-FSE diffusion sequence. The mean fractional anisotropy (as defined in Ref. 27) for all hearts was found to be 0.36 ± 0.09. Figure 4 shows a 3D rendering of the geometry and the corresponding fiber structure of one heart. The heart is colored according to the orientation of the *z*-component of the principle eigenvector. Fibers with circumferential orientation are colored blue, whereas fibers with axial orientation are colored red. The 3D acqui-

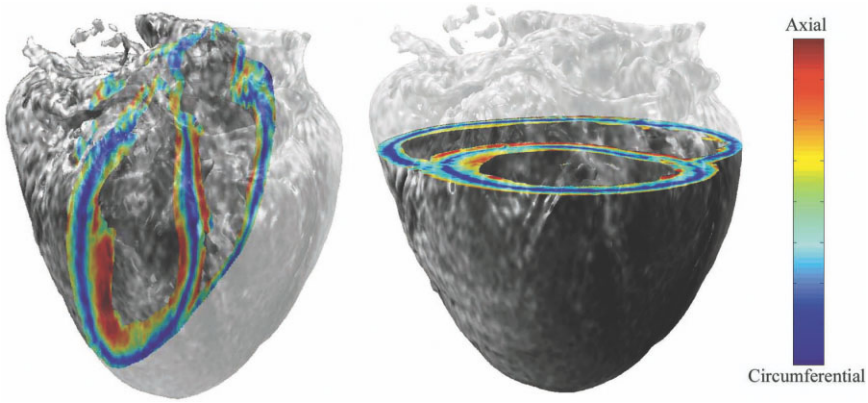

FIG. 4. 3D rendering of the geometry and corresponding fiber structure for one reconstructed heart. The heart is color-coded according to the orientation of the *z*-component of the principle eigenvector. Fibers that run in a circumferential direction are shown in blue, whereas fibers that run in the base–apex direction are colored red.

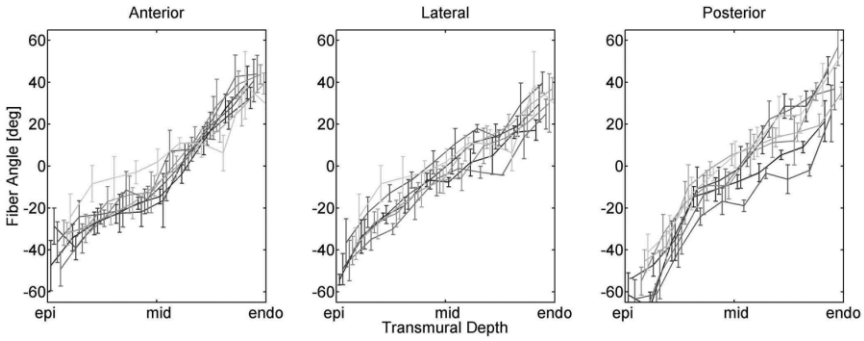

FIG. 5. Transmural variation of the inclination angle for three different regions (the anterior, lateral, and posterior free wall of the LV) for all seven hearts (grayscales). The mean and SD of fiber orientation are evaluated within local regions near each transmural point.

sition scheme enabled us to obtain a higher through-plane resolution of the fiber structure compared to that achieved with the 2D methods.

Before the eigenvectors were studied, a ventricular coordinate system was defined. On average each MR study resulted in 50036 epicardial, 27001 LV endocardial, and 26975 RV endocardial data points, to which the radial component of a 24-element prolate spheroidal FE mesh was fit. The average root mean squared (RMS) errors of the epicardial, LV endocardial, and right ventricular (RV) endocardial surfaces were 0.81 ± 1.08 mm, 0.68 ± 0.83 mm, and 4.48 ± 5.83 mm respectively. The average RMS error of the RV endocardial surface was higher than that of the epicardial and LV endocardial surfaces. The difference in the error may be attributed to the highly trabeculated RV endocardial surface.

Figure 5a–c show fiber inclination angles, θ (see Fig. 3), as a function of transmural depth for three different basal regions: anterior, lateral, and posterior. The mean and standard deviation (SD) of the fiber orientation were evaluated within local regions near each transmural point. The fiber angles ranged from –35.7± 8.6° to 38.5 ± 6.1°, –41.0± 8.0° to 29.7± 6.6°, and –57.0± 6.2° to 39.5 ± 10.6° in the anterior, lateral, and posterior regions, respectively.

To improve our knowledge of DTs and the inferences of tissue structure made from them, we examined the tensor properties from the ventricular wall, where histologic measurements of sheet structure were obtained in previous studies (28–31). In those reports, LV transmural blocks of tissue were isolated and sectioned in ~1 mm increments parallel to the epicardial tangent plane. Measurements of sheet angles were averaged within those sections. Applying a similar approach to our diffusion images we isolated 24 transmural regions by selecting four transmural regions each from within the anterior base, lateral base, posterior base, anterior apex, lateral apex, and posterior apex of the LV. Each of the 24 regions was further sectioned parallel to the epicardial surface into ~1 mm cube subregions, as shown in Fig. 3. Each subregion contained on average of 291 tensor measurements. Given a normalized transmural depth, we assigned each cube as being in the epicardium (0–20%), subepicardium (20–40%), midwall (40–60%), subendocardium (60–80%), or endocardium (80–100%).

Before we analyzed the experimental data, we investigated the power of both the *t*-value and *R*-value under the null hypothesis given a sample size of 291 voxels. Simulations of eigenvalue and eigenvector distributions were performed as described in Materials and Methods. Sets of 291 eigenvalues and eigenvectors were simulated (λ_1 fixed at 1.0×10^{-5} and $\lambda_2 = \lambda_3 = 0.5 \times 10^{-5}$), and our statistical test was applied to each set. Based on the distribution of *t*-values, we determined the critical 1% value for the rejection of the null hypothesis test to be 3.0. The null hypothesis cannot be rejected for *t*-values below this critical value. The critical value for the *R*-test was computed in a similar fashion and determined to be 0.10. These critical values varied slightly with sample size, so further simulations were undertaken and critical values were determined empirically to be inversely related to the square root of the sample size, yielding the following relationships:

$$T_c = \frac{9.00}{\sqrt{n_{samples}}} + 2.53 \qquad R_c = \frac{1.57}{\sqrt{n_{samples}}} + 0.01 \qquad [9]$$

The effects of mean diffusivity tr(**D**)/3 on the critical values of each test are shown in Fig. 6a. Over the range of experimental diffusivities (~0.6×10^{-5} to ~1.3×10^{-5} cm^2/s; gray box in the figure), T_c varied by less than 5%, while R_c showed a greater variability of 36% over the same range.

Next, for each hypothesis test, we explored the effects of Δ on its power (defined as the ratio of the number of test values above its critical value to total samples). Once again, sets of 291 eigenvalues and eigenvectors were simulated, this time with Δs ranging from 0 to 1×10^{-7} cm^2/s. The true diffusivities, λ_1 and λ_3, were held constant (1.0×10^{-5} and 0.5×10^{-5} cm^2/s, respectively) while λ_2 was varied from a value of λ_3 to $\lambda_3 + 1 \times 10^{-6}$. Figure 6b shows the results of these simulations. The power curve for the *t*-test (green), which is not sensitive to the orientation of the primary eigenvector, indicates that the test is more likely to incorrectly accept the null hypothesis H_0 when H_0 is not true for small Δ. It is more likely to correctly reject H_0 when H_0 is false for large Δ. On the other hand, the power curve for the *R*-test, with 5° variation (red) and no variation (orange) in the primary eigenvector, indicates that it is more likely to correctly accept H_0 when H_0 is true for small Δ. However, small variations in the primary eigenvector significantly affect the power of this test at large Δ. On the right axis is plotted the uncertainty (black) of the secondary eigenvectors as a function of Δ. At low Δ the uncertainty in the secondary eigenvector is high, with large variation in the angles, whereas at large Δ the uncer-

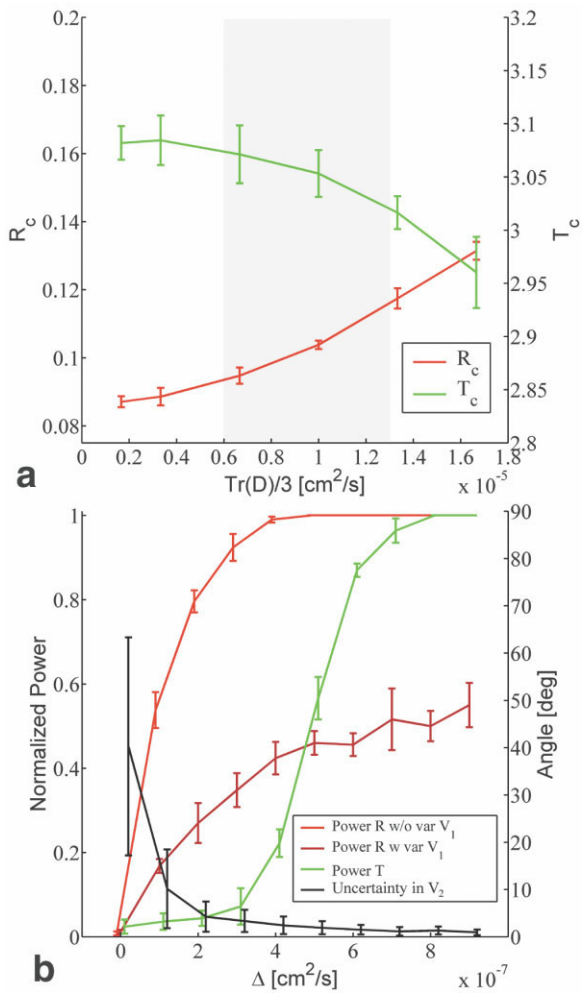

FIG. 6. **a:** Dependence of the mean diffusivity on the critical values for the *t*- and *R*-tests. The shaded region corresponds to the range of experimentally measured diffusivities. **b:** Power of the *R*- and *t*-tests as a function of Δ. The power of the *R*-test is plotted with 5° variation (red) and no variation (orange) in the primary eigenvector direction. The power of the *t*-test (green) is not sensitive to the orientation of the primary eigenvector. On the right axis is plotted the uncertainty of the secondary eigenvectors (black). At low Δ the uncertainty in the secondary eigenvector is large, whereas at large Δ the uncertainty is small.

tainty is low, with small variation in the angles. Even though the *R*-test is more likely to correctly accept H_0 for small Δ, the uncertainty of the eigenvectors in this region is high. Since inferring the tissue microstructure from DTI requires that the eigenvectors have a low uncertainty, we conclude from Fig. 6 that the *t*-test is optimal because it is less sensitive to the mean diffusivity and orientation of the primary eigenvector, and it provides a critical value above which uncertainty in the eigenvectors is low.

Using the *t*-test, we tested the null hypothesis in each of the ventricular subregions. Table 1 shows the results of applying the *t*-test for seven normal canine hearts. Regions in which the average *t*-value was above the critical value are indicated with the symbol *. The vast majority of statistically significant anisotropic regions were located between the subepicardial and subendocardial regions of the anterior, lateral, and posterior regions. These regions showed distinct populations of secondary and tertiary eigenvalues at the $P < 0.01$ level. The consistent *R*-values above 0.10 indicate a nonuniform distribution of eigenvectors, further supporting our proper sorting of the eigenvectors. The *t*-test indicates that no significant distinction between the secondary and tertiary eigenvalues was consistently observed in the epicardial regions, indicating the presence of an isotropic architecture. Though the *R*-test is significant in the epicardial and endocardial regions, where there is larger variation in the primary eigenvector, the uncertainty of the secondary and tertiary eigenvectors is high (Fig. 6).

We used the sorted eigenvectors within those regions for which the null hypothesis was rejected to explore whether their orientation might be an indicator of laminar structure. Figure 7 shows the distribution of intersection angles computed from the tertiary eigenvector in various subregions for two hearts (grayscales). The subplots that do not contain data are regions in which the null hypothesis was accepted. This frequently occurred in the epicardial regions. Within regions where the null hypothesis was rejected, we observed that the majority had a single dominant angle. The value of this dominant angle varied in different regions within the same heart. For example, while all of the apical subepicardial to subendocardial regions of one heart (gray) show dominant angles between

Table 1
Statistical Significance, *T*, of the Secondary and Tertiary Eigenvalues and Uniformity, *R,* of the Secondary Eigenvector as Defined in Methods*

(*T*-value, *R*-value)	Epicardium	Subepicardium	Mid-wall	Subendocardium	Endocardium
Anterior base	2.40 ± 0.11, 0.25 ± 0.01†	2.79 ± 0.16, 0.39 ± 0.06†	2.96 ± 0.19, 0.48 ± 0.03†	3.22 ± 0.43*, 0.37 ± 0.06†	2.96 ± 0.30, 0.29 ± 0.03†
Lateral base	2.55 ± 0.11, 0.21 ± 0.04†	2.76 ± 0.13, 0.45 ± 0.06†	3.00 ± 0.20*, 0.41 ± 0.02†	2.90 ± 0.21 , 0.28 ± 0.02†	2.94 ± 0.31, 0.21 ± 0.03†
Posterior base	2.66 ± 0.20, 0.26 ± 0.08†	2.65 ± 0.28, 0.29 ± 0.03†	2.84 ± 0.33, 0.42 ± 0.02†	3.06 ± 0.36*, 0.38 ± 0.03†	2.92 ± 0.24, 0.35 ± 0.04†
Anterior apex	2.65 ± 0.20, 0.19 ± 0.03†	3.19 ± 0.66*, 0.28 ± 0.07†	3.64 ± 0.68*, 0.32 ± 0.03†	3.51 ± 0.50*, 0.42 ± 0.03†	2.98 ± 0.33, 0.29 ± 0.03†
Lateral apex	2.59 ± 0.17, 0.14 ± 0.03†	3.49 ± 0.84*, 0.24 ± 0.02†	3.43 ± 0.56*, 0.30 ± 0.02†	2.83 ± 0.16 , 0.30 ± 0.02†	2.74 ± 0.19, 0.21 ± 0.02†
Posterior apex	2.74 ± 0.19, 0.24 ± 0.05†	3.09 ± 0.49*, 0.19 ± 0.02†	3.59 ± 0.87*, 0.23 ± 0.02†	3.28 ± 0.50*, 0.32 ± 0.03†	3.10 ± 0.30*, 0.30 ± 0.01†

The symbols * and † indicate significance of *T* value and *R* value, respectively.

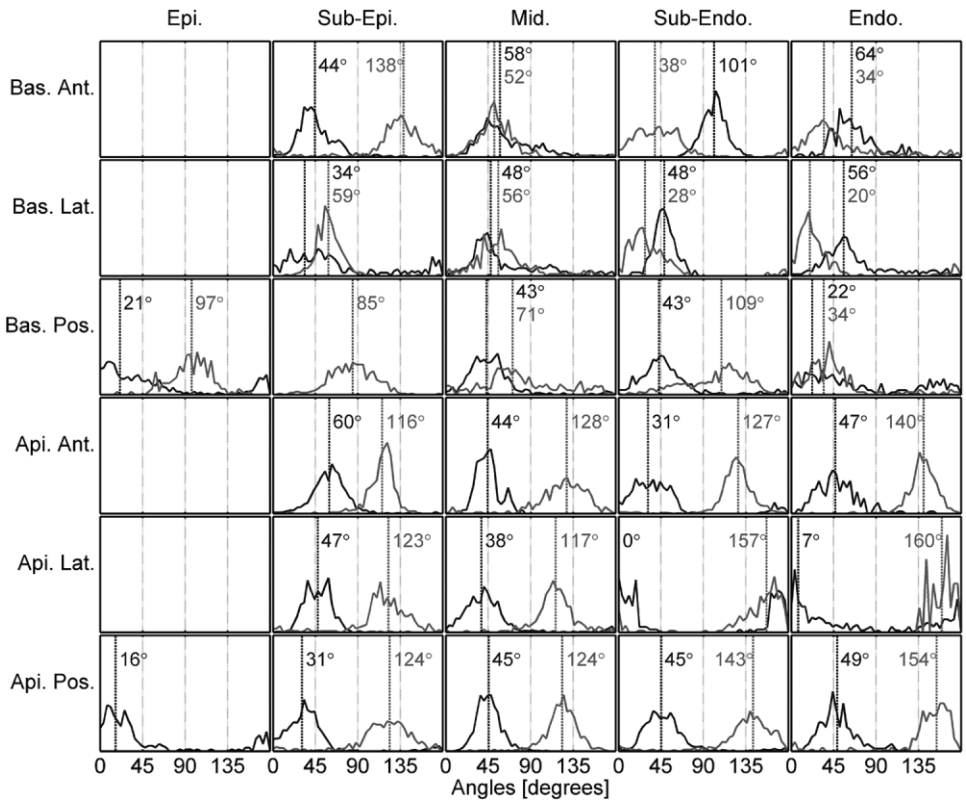

FIG. 7. Histograms of intersection angles computed using the tertiary eigenvector of diffusion in 30 anatomical regions of the LV free wall for two different hearts (grayscales). The subplots that do not contain data are regions in which the null hypothesis was true, and the remaining subplots that do contain data are regions in which the null-hypothesis was rejected.

~110° and 160°, the corresponding basal regions show some dominant angles in this range and others between ~20° and 80°. In the second heart (black), the baso-anterior region shows transmural variation of the dominant angles. It contained similar dominant angles in the subepicardium, mid-wall, and endocardium regions, but a different dominant angle in the subendocardium. Figure 8 shows the pooled distribution of intersection angles taken from the regions where the null hypothesis was rejected for the seven hearts studied. The majority of regions showed bimodal distribution of angles, with averaged values of 45.5° and 117.6°. The basolateral wall showed two populations with a 35° difference between the dominant angles.

DISCUSSION

We have developed and applied a 3D FSE-DTI protocol for estimating DTs at high spatial resolution within the canine ventricular myocardium. This method yields improved imaging of the cardiac ventricular microstructure by eliminating the slice cross-talk effects that occur with 2D imaging methods. The use of a 3D acquisition scheme also enables higher through-plane resolution and therefore enhanced characterization of tissue regions with high fiber curvature, such as the ventricular apex and the RV insertion points.

FE models were used to define a material coordinate system for the analysis of DTI secondary and tertiary eigenvectors. The model accurately characterizes the geometry of both the epicardial and LV endocardial surfaces. The RV endocardial surface has significantly higher error associated with the fit due to the large degree of trabeculation. Most of the error is located near the RV junctions, which are difficult to model with Hermitian elements.

A hypothesis-testing procedure for identifying regions of myocardium that exhibit either transverse isotropy or anisotropy of diffusion was developed. Our statistical method was based solely on the difference between the secondary and tertiary eigenvalues. In brain imaging, the secondary and tertiary eigenvalues provide information on fiber tract crossings and/or diverging fiber tracts (32). In the heart, they are hypothesized to provide information on the 3D structure of laminar architecture (11).

Our data provide strong evidence that the tertiary eigenvector defines the sheet normal. First, we found that regions between the subepicardium and endocardium exhibit greater anisotropy than the epicardial regions. This transmural change in myocardial anisotropy may be attributed to transmural variation in the sheet structure. Connective tissue bundles myocytes together to form laminar sheets. Adjacent laminar sheets are in turn coupled with long collagen fibers (33). LeGrice et al. (31) reported that coupling between layers decreased twofold from the subepicardium to the mid-wall, whereas the length of collagen fibers connecting muscle layers was greatest in the mid-wall. It has also been observed that within the subepicardial to subendocardial regions, local wall thickening increases significantly (1,34–36), a finding that has been attributed to the local structure and function of the laminar sheets (2,30). Our observed transmural variation in anisotropy together with observations of transmural variation in sheet coupling and dynamics from the cardiac-mechanics literature suggest a possible link between diffusion anisotropy and sheet structure.

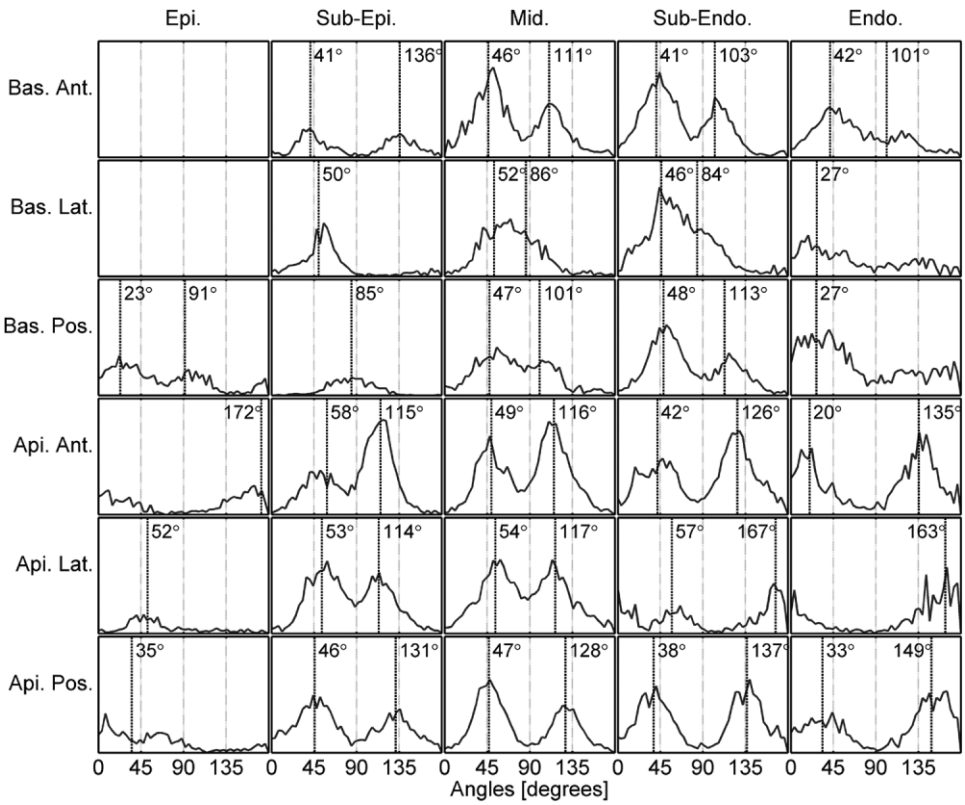

FIG. 8. Histograms of pooled intersection angles computed using the tertiary eigenvector of diffusion in 30 anatomical regions of the LV free wall for seven hearts. The subplots that do not contain data are regions in which the null hypothesis was true, and the remaining subplots that do contain data are regions in which the null-hypothesis was rejected.

Second, in each of the study hearts the majority of regions contained a dominant angle within the distribution of intersection angles, ϕ (see Fig. 3). This dominant angle differed at various anatomic regions. These findings are strikingly similar to histological results reported by others (28–30,37,38) indicating the presence of a dominant muscle layer. Many of those reports also indicated the presence of different dominant muscle layers within the same heart at different transmural depths.

Third, using circular statistics, we found that the dominant populations were located at approximately 45° and 117°. Histological measurements have indicated similar values for sheet angles. Dokos et al. (38) identified a dominant mid-wall muscle layer at ~45° and another at ~135°. Ashikaga et al. (29) observed angles at 36° and another at ~70–90° apart. Fourth, when the distribution angles for all of our seven hearts were pooled, a bimodal distribution of angles per location emerged (Fig. 8). The two dominant angles were equally likely. Arts et al. (28) pooled histological measurements from six canine hearts and observed angles at 45° and 135° per location with similar likelihood, and supported their measurements using theoretical models of cardiac mechanics. Finally, we found that the difference between the two dominant populations was 35–115° with a mean difference of 78°. Coupling this observation with the significant *t*-values eliminates the possibility that the dominant angles are due to erroneous selection of the secondary and tertiary eigenvectors. The consistency between our results and histological reports strongly suggests that the tertiary eigenvector corresponds to the sheet normal.

CONCLUSIONS

We have described an improved method for 3D FSE DTI of the cardiac ventricles, and a novel method for testing the hypothesis that secondary and tertiary eigenvalues may be distinguished with high confidence ($P < 0.01$). Using these methods, we produced strong supportive evidence that the tertiary eigenvector defines a surface normal to the cardiac laminar sheets. Collectively, the hearts demonstrate that two populations of laminar orientations are equally possible for the various regions, most notably the anterior and posterior regions. A fundamental understanding of the cardiac microstructure is of great importance, and the knowledge gained from these datasets will be incorporated into current working models of electrical and mechanical activation in both diseased and failing hearts.

REFERENCES

1. Waldman LK, Nosan D, Villarreal F, Covell JW. Relation between transmural deformation and local myofiber direction in canine left ventricle. Circ Res 1988;63:550–562.
2. Takayama Y, Costa KD, Covell JW, McCulloch AD. Contribution of laminar myofiber architecture to load-dependent changes in mechanics of LV myocardium. Am J Physiol Heart Circ Physiol 2002;282:H1510–1520.
3. Colli Franzone P, Guerri L, Pennacchio M, Taccardi B. Spread of excitation in 3-D models of the anisotropic cardiac tissue. III. Effects of ventricular geometry and fiber structure on the potential distribution. Math Biosci 1998;151:51–98.
4. Roberts DE, Hersh LT, Scher AM. Influence of cardiac fiber orientation on wavefront voltage, conduction velocity, and tissue resistivity in the dog. Circ Res 1979;44:701–712.
5. Taccardi B, Macchi E, Lux RL, Ershler PR, Spaggiari S, Baruffi S, Vyhmeister Y. Effect of myocardial fiber direction on epicardial potentials. Circulation 1994;90:3076–3090.

6. Anderson KP, Walker R, Urie P, Ershler PR, Lux RL, Karwandee SV. Myocardial electrical propagation in patients with idiopathic dilated cardiomyopathy. J Clin Invest 1993;92:122–140.
7. Basser PJ, Mattiello J, LeBihan D. Estimation of the effective self-diffusion tensor from the NMR spin echo. J Magn Reson B 1994;103: 247–254.
8. Scollan DF, Holmes A, Winslow R, Forder J. Histological validation of myocardial microstructure obtained from diffusion tensor magnetic resonance imaging. Am J Physiol 1998;275:H2308–H2318.
9. Hsu EW, Muzikant AL, Matulevicius SA, Penland RC, Henriquez CS. Magnetic resonance myocardial fiber-orientation mapping with direct histological correlation. Am J Physiol 1998;274:H1627–H1634.
10. Holmes AA, Scollan DF, Winslow RL. Direct histological validation of diffusion tensor MRI in formaldehyde-fixed myocardium. Magn Reson Med 2000;44:157–161.
11. Scollan DF, Holmes A, Zhang J, Winslow RL. Reconstruction of cardiac ventricular geometry and fiber orientation using magnetic resonance imaging. Ann Biomed Eng 2000;28:934–944.
12. Tseng WY, Wedeen VJ, Reese TG, Smith RN, Halpern EF. Diffusion tensor MRI of myocardial fibers and sheets: correspondence with visible cut-face texture. J Magn Reson Imaging 2003;17:31–42.
13. Pierpaoli C, Basser PJ. Toward a quantitative assessment of diffusion anisotropy. Magn Reson Med 1996;36:893–906.
14. Basser PJ, Pajevic S. Statistical artifacts in diffusion tensor MRI (DT-MRI) caused by background noise. Magn Reson Med 2000;44:41–50.
15. Garrido L, Wedeen VJ, Kwong KK, Spencer UM, Kantor HL. Anisotropy of water diffusion in the myocardium of the rat. Circ Res 1994;74:789–793.
16. Faris OP, Evans FJ, Ennis DB, Helm PA, Taylor JL, Chesnick AS, Guttman MA, Ozturk C, McVeigh ER. Novel technique for cardiac electromechanical mapping with magnetic resonance imaging tagging and an epicardial electrode sock. Ann Biomed Eng 2003;31:430–440.
17. Streeter Jr DD, Spotnitz HM, Patel DP, Ross Jr J, Sonnenblick EH. Fiber orientation in the canine left ventricle during diastole and systole. Circ Res 1969;24:339–347.
18. Hennig J, Nauerth A, Friedburg H. RARE imaging: a fast imaging method for clinical MR. Magn Reson Med 1986;3:823–833.
19. Hennig J, Friedburg H, Ott D. Fast three-dimensional imaging of cerebrospinal fluid. Magn Reson Med 1987;5:380–383.
20. Brockstedt S, Thomsen C, Wirestam R, Holtas S, Stahlberg F. Quantitative diffusion coefficient maps using fast spin-echo MRI. Magn Reson Imaging 1998;16:877–886.
21. LeGrice IJ, Hunter PJ, Smaill BH. Laminar structure of the heart: a mathematical model. Am J Physiol 1997;272:H2466–2476.
22. Anderson TW. An introduction to multivariate statistical analysis. New York: John Wiley & Sons; 1984.
23. Sheskin DJ. Handbook of parametric and nonparametric statistical procedures. New York: CRC Press, Inc; 1997.
24. Nielsen PM, LeGrice IJ, Smaill BH, Hunter PJ. Mathematical model of geometry and fibrous structure of the heart. Am J Physiol 1991;260: H1365–1378.
25. Terzopoulos D. Regularization of inverse visual problems involving discontinuities. IEEE Trans Patt Anal Machine Intel 1989;8:413–424.
26. Fisher NI. Statistical analysis of circular data. New York: Cambridge University Press; 1993.
27. Basser PJ. Inferring microstructural features and the physiological state of tissues from diffusion-weighted images. NMR Biomed 1995;8:333–344.
28. Arts T, Costa KD, Covell JW, McCulloch AD. Relating myocardial laminar architecture to shear strain and muscle fiber orientation. Am J Physiol Heart Circ Physiol 2001;280:H2222–H2229.
29. Ashikaga H, Criscione JC, Omens JH, Covell JW, Ingels Jr NB. Transmural left ventricular mechanics underlying torsional recoil during relaxation. Am J Physiol Heart Circ Physiol 2004;286:H640–H647.
30. Costa KD, Takayama Y, McCulloch AD, Covell JW. Laminar fiber architecture and three-dimensional systolic mechanics in canine ventricular myocardium. Am J Physiol 1999;276:H595–607.
31. LeGrice IJ, Smaill BH, Chai LZ, Edgar SG, Gavin JB, Hunter PJ, Takayama Y, Covell JW. Laminar structure of the heart: ventricular myocyte arrangement and connective tissue architecture in the dog. Am J Physiol 1995;269:H571–H582.
32. Wiegell MR, Larsson HB, Wedeen VJ. Fiber crossing in human brain depicted with diffusion tensor MR imaging. Radiology 2000;217:897–903.
33. Caulfield JB, Borg TK. The collagen network of the heart. Lab Invest 1979;40:364–372.
34. Sabbah HN, Marzilli M, Stein PD. The relative role of subendocardium and subepicardium in left ventricular mechanics. Am J Physiol 1981; 240:H920–H926.
35. Rademakers FE, Rogers WJ, Guier WH, Hutchins GM, Siu CO, Weisfeldt ML, Weiss JL, Shapiro EP. Relation of regional cross-fiber shortening to wall thickening in the intact heart. Three-dimensional strain analysis by NMR tagging. Circulation 1994;89:1174–1182.
36. Gallagher KP, Osakada G, Matsuzaki M, Miller M, Kemper WS, Ross Jr J. Nonuniformity of inner and outer systolic wall thickening in conscious dogs. Am J Physiol 1985;249:H241–248.
37. Young AA, LeGrice IJ, Young MA, Smaill BH. Extended confocal microscopy of myocardial laminae and collagen network. J Microsc 1998; 192:139–150.
38. Dokos S, Smaill BH, Young AA, LeGrice IJ. Shear properties of passive ventricular myocardium. Am J Physiol Heart Circ Physiol 2002;283: H2650–H2659.